OPTICAL REVIEW Vol. 21, No. 5 (2014) 568–575

Simulation on Near-Field Light Generated by Metal Nano-Dot on GaAs Substrate for Heat Source of Heat-Assisted Magnetic Recording

Ryuichi KATAYAMA*

Department of Information Electronics, Faculty of Engineering, Fukuoka Institute of Technology, Fukuoka 811-0295, Japan

(Received November 30, 2013; Accepted May 15, 2014)

Heat-assisted magnetic recording (HAMR) is promising for achieving more than 1 Tb/inch^2 recording density. A near-field transducer (NFT), which forms a hot spot of 10–100 nm in diameter on a recording medium, is necessary in HAMR. In this study, localized surface plasmons generated by a metal nano-dot in a novel device for a heat source of heat-assisted magnetic recording were analyzed using a simple model in which a metal hemisphere was formed on a GaAs substrate and a quasi-electrostatic approximation. The scattering and absorption efficiencies as well as the enhancement factor were investigated for several kinds of metal. As a result, their dependence on the wavelength and the polarization direction of the incident light was clarified.

Keywords: heat-assisted magnetic recording, near-field transducer, near-field light, localized surface plasmon, metal nano-dot, quasi-electrostatic approximation

1. Introduction

In the present information explosion era, the recording density of hard disk drives is increasing by 40%/year and has reached 700 Gb/inch^2. However, to record a smaller mark stably on a recording medium, the recording medium needs to have higher coercivity, thereby requiring a higher magnetic field intensity for recording, which is difficult to obtain using a conventional magnetic recording head. To overcome this difficulty and to achieve a more than 1 Tb/inch^2 recording density, a novel technology must be introduced. Heat-assisted magnetic recording[1] (HAMR) is a promising technology for this purpose. In HAMR, the recording medium is heated locally by a light spot smaller than the diffraction limit to reduce the coercivity and to enable the mark to be recorded using the conventional magnetic recording head. Therefore, a near-field transducer (NFT), which forms such a hot spot of 10–100 nm in diameter on the recording medium, is necessary, and various types of NFTs such as Lollipop type[2] and E-antenna type[3] were previously proposed. However, these NFTs involve a concern that the heat generated by the NFT would melt the NFT itself when the recording density becomes higher and the size of the hot spot becomes smaller.

To solve this issue, a novel device for a HAMR heat source was proposed by Kuriyama et al. in 2013.[4] Figure 1 shows the structure of the proposed device. This device has a Au nano-dot as the NFT, which is formed on a GaAs mesa containing InAs quantum dots. It is expected that the NFT can be kept cool thanks to the heat sinking effect of the GaAs mesa even if the size of the hot spot becomes smaller. The objective of this study is to analyze the localized surface plasmons generated by such a metal nano-dot and to investigate the scattering and absorption by the metal nano-dot as well as the distribution of near-field light through a numerical simulation for the purpose of optimizing the structure of this device.

*E-mail address: r-katayama@fit.ac.jp

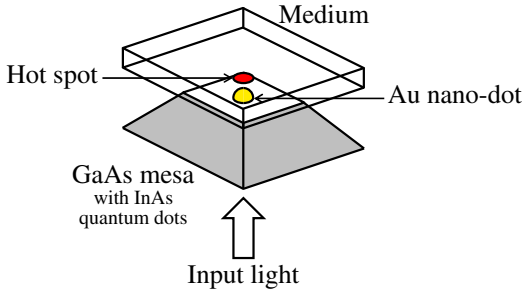

Fig. 1. (Color online) Structure of proposed device for HAMR heat source.

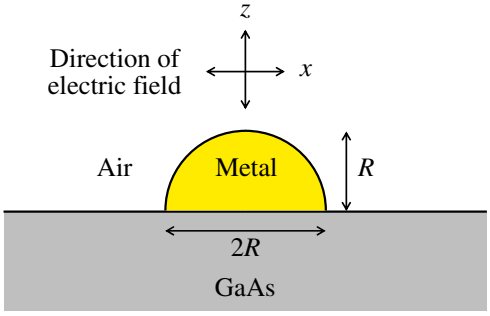

Fig. 2. (Color online) Simulation model.

2. Simulation Methods

Figure 2 shows the simulation model. A metal nano-hemisphere with radius R is formed on a GaAs substrate. An x–y plane was defined parallel to the surface of the GaAs substrate and a z-axis was defined perpendicular to it. A uniform external electric field in the GaAs substrate was assumed, which corresponds to the case that a plane wave was incident on the metal nano-dot from the GaAs substrate. First, the scattering and absorption efficiencies by the metal

nano-dot (Q_{sca} and Q_{abs}) were calculated, which were respectively defined as the cross-sections of the incident light whose power is equal to the power of the scattered and absorbed lights by the metal nano-dot divided by the base area of the metal nano-dot. The near-field scattering efficiency by the metal nano-dot (Q_{nf}) was also calculated, which was defined as the power of the near-field light integrated over the surface of the metal nano-dot divided by the power of the incident light integrated over the base of the metal nano-dot. Next, the intensity and polarization distributions of the near-field light generated by the metal nano-dot were calculated. Finally, the enhancement factor of the light intensity ($|E/E_0|^2$) was calculated, where E_0 represents the amplitude of the incident light and E represents the sum of the amplitude of the near-field light and that of the transmitted light at the top of the metal nano-dot.

A quasi-electrostatic approximation[5] was used in the simulation. This approximation is valid if R is sufficiently smaller than the wavelength of the incident light and the electric field in the metal nano-dot is considered to be uniform. In the quasi-electrostatic approximation, the external electric field and the induced electric field by the polarization of the metal were expressed using a multipole expansion in each region and expansion coefficients were calculated from boundary conditions between the regions. The direction of the external electric field corresponding to the polarization direction of the incident light was either the x- or z-direction. Actually, the incident light cannot be purely z-polarized and generally contains both x- and z-polarization components because it is incident from the substrate. However, if we understand the characteristics of the near-field light generated by the metal nano-dot for the x- and z-polarized light, we can also understand those for an obliquely polarized light by combining those for the two polarization components. The wavelength of the incident light was varied between 300 and 1800 nm. Gold (Au), silver (Ag), copper (Cu), and platinum (Pt) were chosen as the metals for the nano-dot. The dielectric constants of the metals and GaAs shown in Ref. 6 were used, which means that the dependence of the dielectric constants on R was not considered.

The potentials expressed using the multipole expansion when the incident light is x- and z-polarized are given by Eqs. (1)–(3) and Eqs. (4)–(6), respectively. Here, ψ_0, ψ_1, and ψ_2 represent the potentials corresponding to the external electric field in the GaAs substrate, the induced electric field in the air, and the induced electric field in the metal nano-dot, respectively. Polar coordinates are used in the equations, P_{j0} and P_{j1} are associated Legendre functions, and A_{1j}, A_{2j}, B_{1j}, and B_{2j} are the expansion coefficients.

$$\psi_0 = r\sin\theta\cos\varphi, \tag{1}$$

$$\psi_1 = \sum_{j=1}^{\infty} B_{1j} r^{-j-1} P_j^1(\cos\theta)\cos\varphi, \tag{2}$$

$$\psi_2 = \sum_{j=1}^{\infty} B_{2j} r^{j} P_j^1(\cos\theta)\cos\varphi, \tag{3}$$

$$\psi_0 = r\cos\theta, \tag{4}$$

$$\psi_1 = \sum_{j=1}^{\infty} A_{1j} r^{-j-1} P_j^0(\cos\theta), \tag{5}$$

$$\psi_2 = \sum_{j=1}^{\infty} A_{2j} r^{j} P_j^0(\cos\theta). \tag{6}$$

If the incident light is obliquely polarized with the angle between the polarization direction and the z-direction being θ_0, the potentials are given by Eqs. (7)–(9):

$$\psi_0 = r\cos\theta\cos\theta_0 + r\sin\theta\sin\theta_0\cos\varphi, \tag{7}$$

$$\psi_1 = \sum_{j=1}^{\infty}\{A_{1j} r^{-j-1} P_j^0(\cos\theta) + B_{1j} r^{-j-1} P_j^1(\cos\theta)\cos\varphi\}, \tag{8}$$

$$\psi_2 = \sum_{j=1}^{\infty}\{A_{2j} r^{j} P_j^0(\cos\theta) + B_{2j} r^{j} P_j^1(\cos\theta)\cos\varphi\}. \tag{9}$$

3. Simulation Results

Figures 3 and 4 show the calculated scattering and absorption efficiencies versus wavelength characteristics, respectively. The metals for the nano-dot are Au in Figs. 3(a), 3(b), 4(a), and 4(b); Ag in Figs. 3(c), 3(d), 4(c), and 4(d); Cu in Figs. 3(e), 3(f), 4(e), and 4(f); and Pt in Figs. 3(g), 3(h), 4(g), and 4(h). The incident light is x-polarized in Figs. 3(a), 3(c), 3(e), 3(g), 4(a), 4(c), 4(e), and 4(g), while it is z-polarized in Figs. 3(b), 3(d), 3(f), 3(h), 4(b), 4(d), 4(f), and 4(h). The horizontal axis in Figs. 3 and 4 indicates the wavelength of the incident light. The vertical axis in Fig. 3 indicates the scattering efficiency normalized by R^4 and that in Fig. 4 indicates the absorption efficiency normalized by R. The reason why they were normalized is that the scattering efficiency is proportional to R^4 and the absorption efficiency is proportional to R when the quasi-electrostatic approximation is used and the dependence of the dielectric constants on R is not considered. The surface plasmon resonance wavelengths for the x- and z-polarized incident light at which the efficiencies became maximum were around 850 and 430 nm, respectively, for Au; around 840 and 360 nm, respectively, for Ag; around 860 and 430 nm, respectively, for Cu; and around 650–660 and 400–430 nm, respectively, for Pt. No sharp peak was observed in Figs. 3(g) and 4(g).

Figure 5 shows the calculated near-field scattering efficiency versus wavelength characteristics. The metals for the nano-dot are Au in Figs. 5(a) and 5(b), Ag in Figs. 5(c) and 5(d), Cu in Figs. 5(e) and 5(f), and Pt in Figs. 5(g) and 5(h). The incident light is x-polarized in Figs. 5(a), 5(c), 5(e), and 5(g), while it is z-polarized in Figs. 5(b), 5(d), 5(f), and 5(h). The horizontal axis indicates the wavelength of the incident light and the vertical axis indicates the near-field scattering efficiency. The near-field scattering efficiency for Au for the x-polarized incident light had a peak at around 850 nm, which was similar to the scattering and absorption efficiencies. On the other hand, that for the z-polarized incident light had two peaks at around 430 and 520 nm, as shown in Fig. 5(b), which was different from the scattering and absorption efficiencies

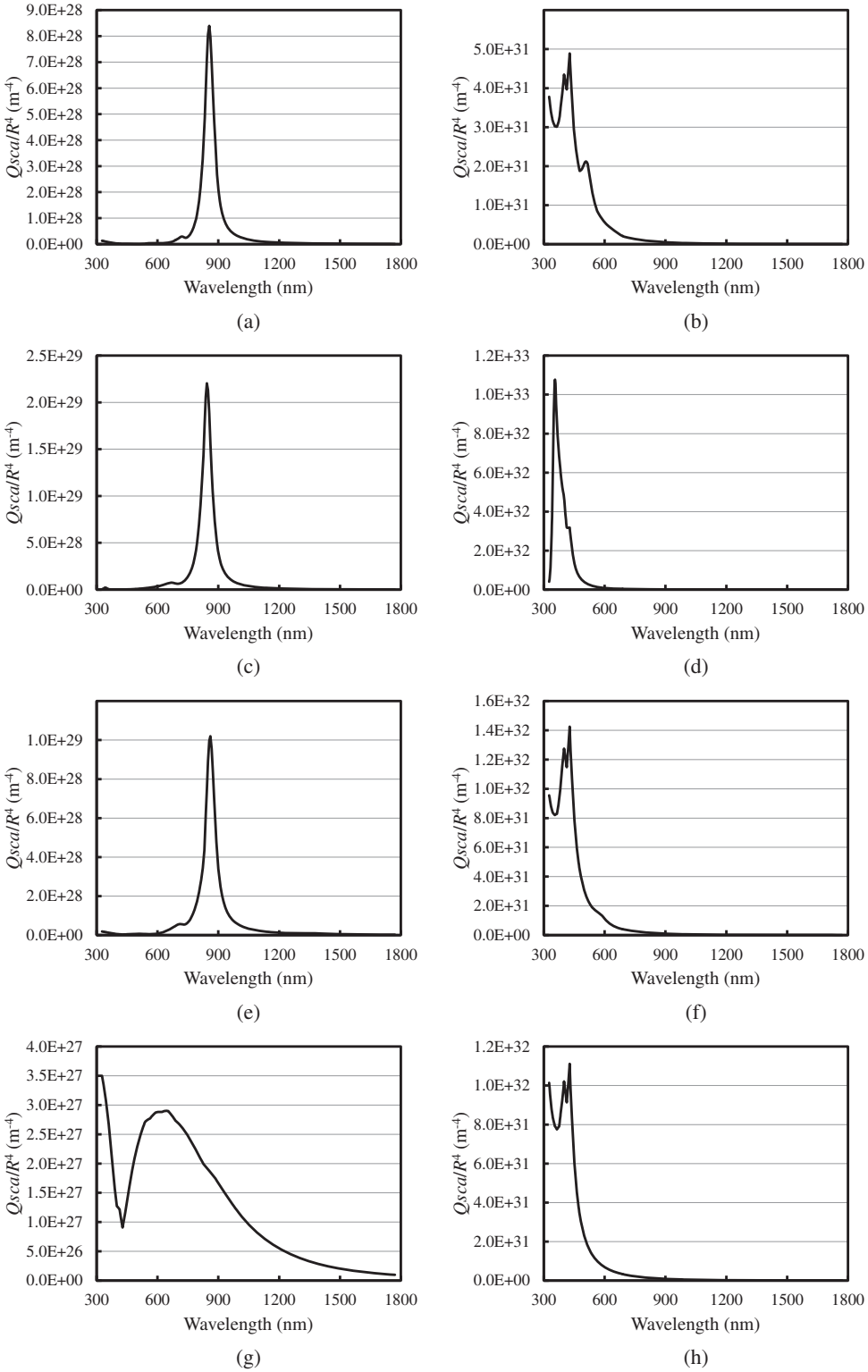

Fig. 3. Calculated scattering efficiency versus wavelength characteristics: (a) Au, *x*-polarized light, (b) Au, *z*-polarized light, (c) Ag, *x*-polarized light, (d) Ag, *z*-polarized light, (e) Cu, *x*-polarized light, (f) Cu, *z*-polarized light, (g) Pt, *x*-polarized light, and (h) Pt, *z*-polarized light.

where the second peak was not so distinct. The near-field scattering efficiencies for the *x*- and *z*-polarized incident light had a peak at around 840 and 360 nm, respectively, for Ag; around 860 and 430 nm, respectively, for Cu; and around 1030 and 430 nm, respectively, for Pt. No sharp peak was observed in Fig. 5(g), and the peak position in Fig. 5(g) was different from those in Figs. 3(g) and 4(g).

Figures 6–8 show the calculated intensity and polarization distributions of near-field light generated by the metal nano-dot, when the metal for the nano-dot is Au. In Fig. 6, the

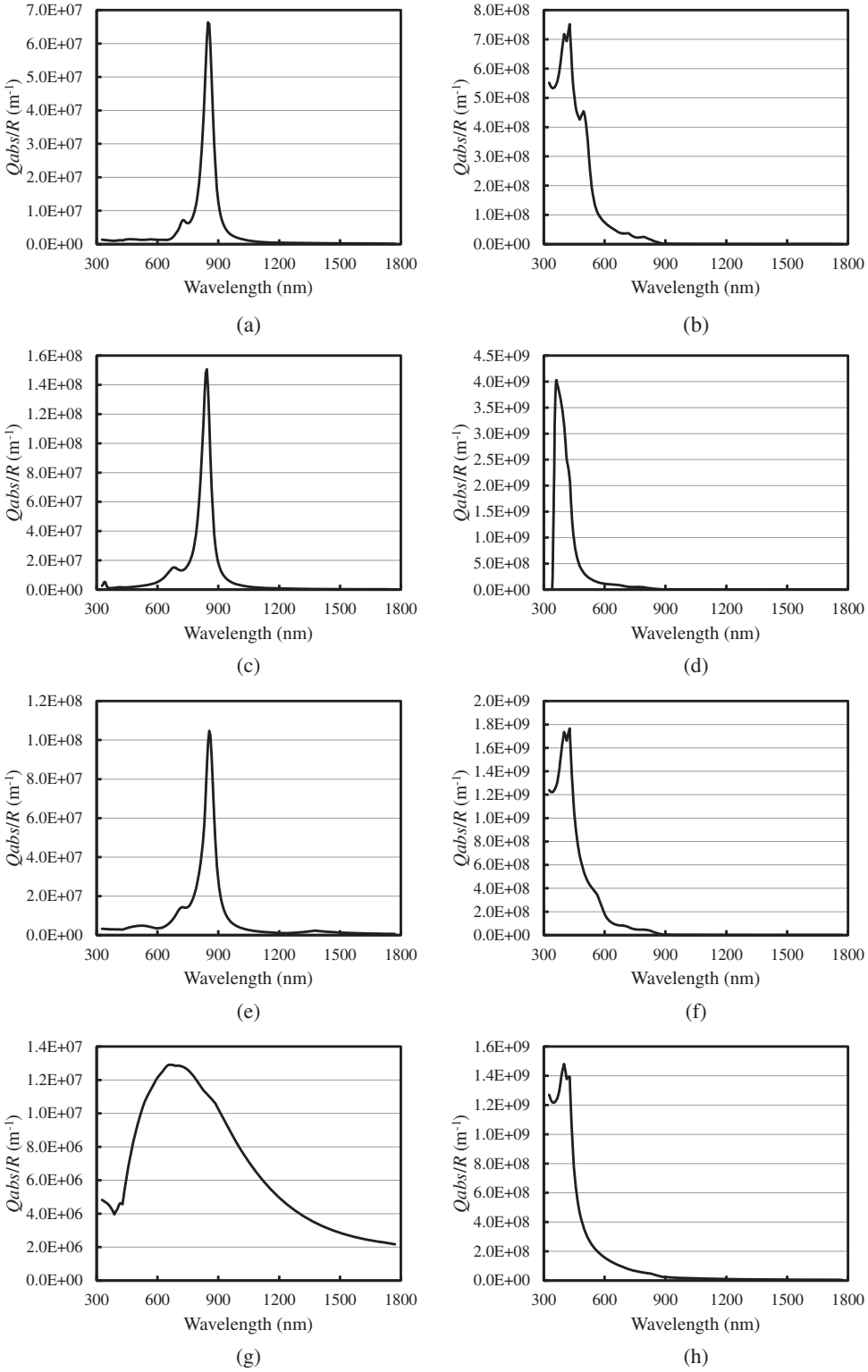

Fig. 4. Calculated absorption efficiency versus wavelength characteristics: (a) Au, *x*-polarized light, (b) Au, *z*-polarized light, (c) Ag, *x*-polarized light, (d) Ag, *z*-polarized light, (e) Cu, *x*-polarized light, (f) Cu, *z*-polarized light, (g) Pt, *x*-polarized light, and (h) Pt, *z*-polarized light.

incident light is *x*-polarized and its wavelength is 850 nm. In Fig. 7, the incident light is *z*-polarized and its wavelength is 430 nm. In Fig. 8, the incident light is *z*-polarized and its wavelength is 520 nm. The intensity distributions are shown in Figs. 6(a), 7(a), and 8(a), while the polarization distributions are shown in Figs. 6(b), 7(b), and 8(b). Here, the intensity of the near-field light was normalized by that of the incident light. The intensity was high at the side of the Au dot for the *x*-polarized incident light and at the top of the Au dot for the *z*-polarized incident light. Consequently, the

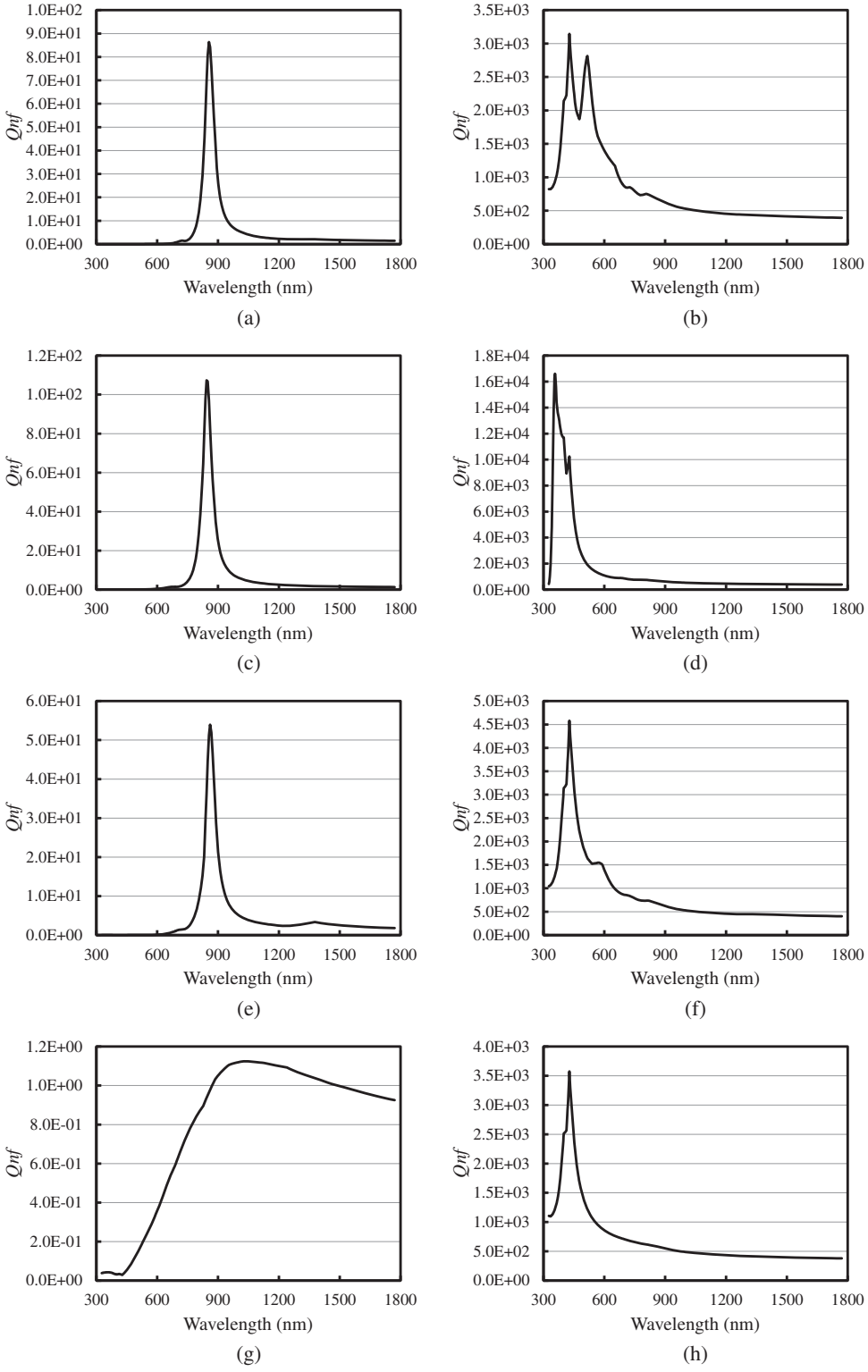

Fig. 5. Calculated near-field scattering efficiency versus wavelength characteristics: (a) Au, *x*-polarized light, (b) Au, *z*-polarized light, (c) Ag, *x*-polarized light, (d) Ag, *z*-polarized light, (e) Cu, *x*-polarized light, (f) Cu, *z*-polarized light, (g) Pt, *x*-polarized light, and (h) Pt, *z*-polarized light.

intensity at the top of the Au dot was relatively low for the *x*-polarized incident light and relatively high for the *z*-polarized incident light.

Figure 9 shows the calculated enhancement factor versus wavelength characteristics. The metals for the nano-dot are Au in Figs. 9(a) and 9(b), Ag in Figs. 9(c) and 9(d), Cu in Figs. 9(e) and 9(f), and Pt in Figs. 9(g) and 9(h). The incident light is *x*-polarized in Figs. 9(a), 9(c), 9(e), and 9(g), while it is *z*-polarized in Figs. 9(b), 9(d), 9(f), and 9(h). The horizontal axis indicates the wavelength of the incident light

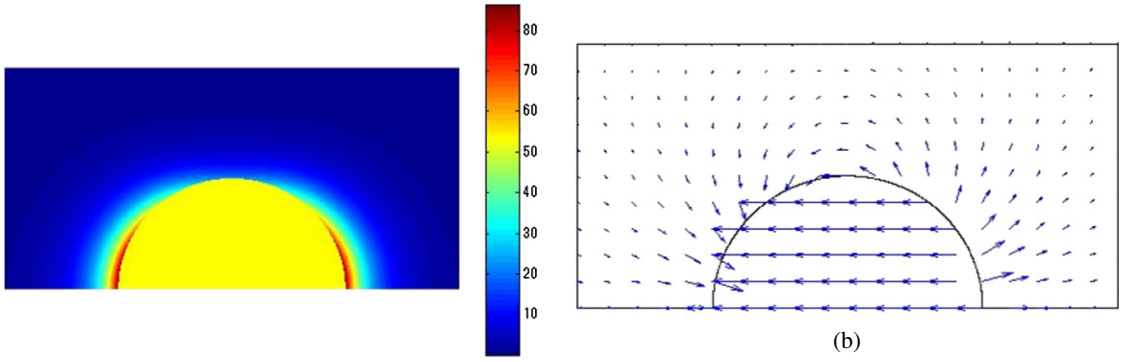

(a) (b)

Fig. 6. (Color online) Calculated distribution of near-field light generated by Au nano-dot for *x*-polarized light at 850 nm: (a) intensity distribution and (b) polarization distribution.

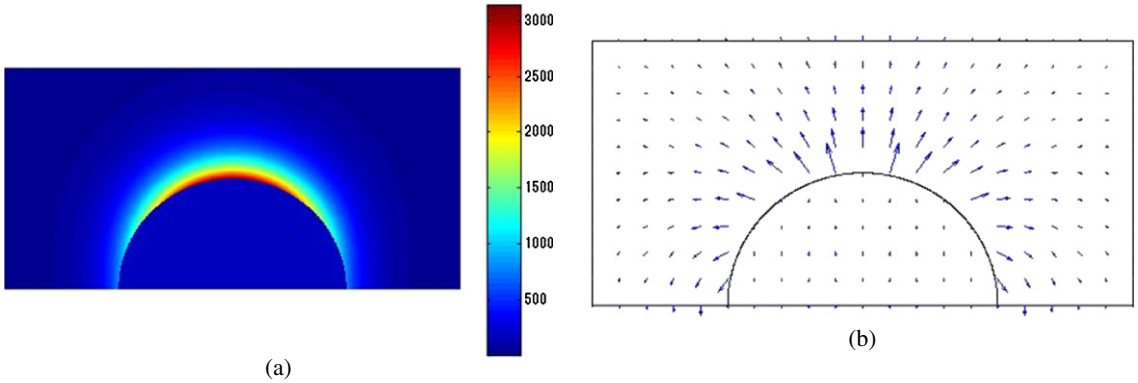

(a) (b)

Fig. 7. (Color online) Calculated distribution of near-field light generated by Au nano-dot for *z*-polarized light at 430 nm: (a) intensity distribution and (b) polarization distribution.

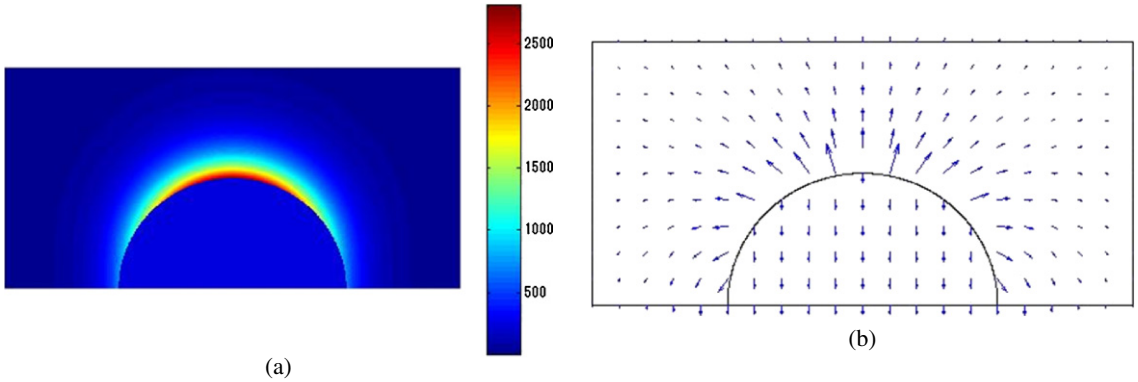

(a) (b)

Fig. 8. (Color online) Calculated distribution of near-field light generated by Au nano-dot for *z*-polarized light at 520 nm: (a) intensity distribution and (b) polarization distribution.

and the vertical axis indicates the enhancement factor. The enhancement factor for Au for the *x*-polarized incident light had a peak at around 850 nm and that for the *z*-polarized incident light had two peaks at around 430 and 520 nm, which were similar to the case of the near-field scattering efficiency. The enhancement factors for the *x*- and *z*-polarized incident light had a peak at around 840 and 360 nm, respectively, for Ag; around 860 and 430 nm, respectively, for Cu; and around 500 and 430 nm, respectively, for Pt. No sharp peak was observed in Fig. 9(g), and the peak position in Fig. 9(g) was different from those in Figs. 3(g), 4(g), and 5(g). The enhancement factor for Au for the *x*-polarized incident light at the wavelength of 850 nm was about 21, and those for the *z*-polarized incident light at the wavelengths of 430 and 520 nm were about 6800 and 4900, respectively. The enhancement factor for Ag for the *x*-polarized incident light at the wavelength of 840 nm was about 26, and that for the *z*-polarized incident light at the

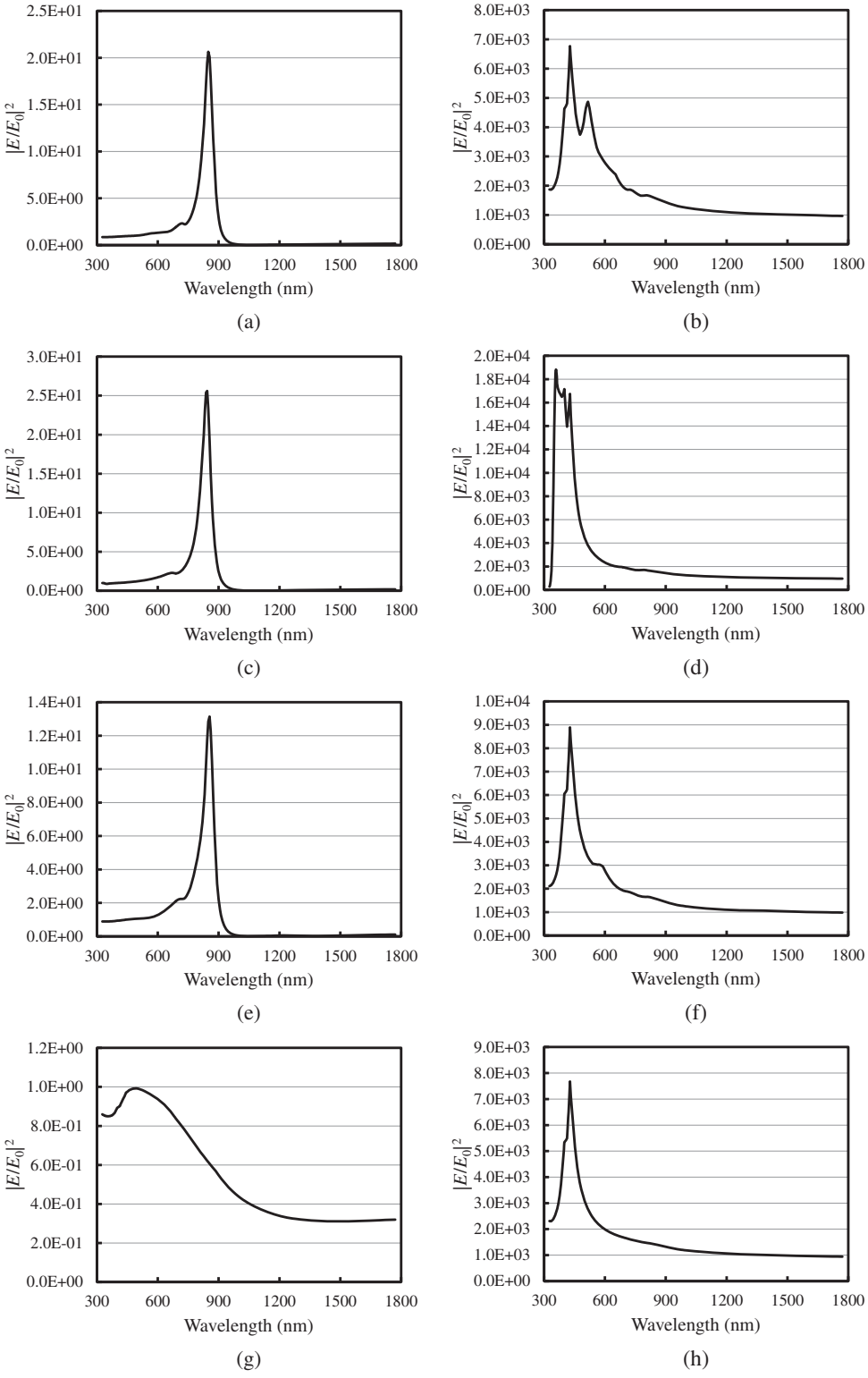

Fig. 9. Calculated enhancement factor versus wavelength characteristics: (a) Au, *x*-polarized light, (b) Au, *z*-polarized light, (c) Ag, *x*-polarized light, (d) Ag, *z*-polarized light, (e) Cu, *x*-polarized light, (f) Cu, *z*-polarized light, (g) Pt, *x*-polarized light, and (h) Pt, *z*-polarized light.

wavelength of 360 nm was about 19000. The enhancement factor for Cu for the *x*-polarized incident light at the wavelength of 860 nm was about 13, and that for the *z*-polarized incident light at the wavelength of 430 nm was about 8900. The enhancement factor for Pt for the *x*-polarized incident light at the wavelength of 500 nm was about 0.99, and that for the *z*-polarized incident light at the wavelength of 430 nm was about 7700.

4. Discussion

First, the scattering and absorption efficiencies are discussed. As shown in Figs. 3 and 4, the wavelength dependence of the scattering efficiency and that of the absorption efficiency were similar to each other. The scattering and absorption efficiencies for the x-polarized incident light were relatively low and those for the z-polarized incident light were relatively high for each metal. These were caused by the difference in the boundary conditions between the regions. As explained in the next paragraph, the electric field intensity in the air is not enhanced for the x-polarized light while it is enhanced for the z-polarized light. This means that both the real and imaginary parts of A_{11} in Eq. (5) are larger than those of B_{11} in Eq. (2). Since the polarizability of Au (α) is proportional to B_{11} and A_{11} for the x- and z-polarized incident light, respectively, both the real and imaginary parts of α for the z-polarized incident light are larger than those for the x-polarized incident light. The scattering efficiency is proportional to the square of the absolute value of α and the absorption efficiency is proportional to the imaginary part of α. Therefore, it is understood that the scattering and absorption efficiencies for the z-polarized incident light are higher than those for the x-polarized incident light. Moreover, the wavelength dependence of the scattering and absorption efficiencies for the x-polarized incident light and that for the z-polarized incident light were quite different from each other for each metal. This led to the difference in the surface plasmon resonant wavelengths.

Next, the enhancement factor is discussed. As shown in Fig. 9, the enhancement factor for the x-polarized incident light was typically on the order of 10^1, which was relatively small, while that for the z-polarized incident light was typically on the order of 10^3, which was relatively large. This was also caused by the difference in the boundary conditions between the regions. For the x-polarized light, the tangential component of the electric field is continuous between the regions. Therefore, the electric field intensity is not enhanced. On the other hand, for the z-polarized light, the normal component of the electric flux density (the product of the dielectric constant and the electric field) is continuous between the regions. Therefore, if the dielectric constant of the input region is 10 times larger than that of the output region, the electric field intensity of the output region is enhanced by 10^2 times compared with that of the input region. Consequently, the z-polarized incident light is preferable for this novel device for the HAMR heat source. Among the four kinds of metal used for the nano-dot, Ag has the highest enhancement factor and Au, Cu, and Pt have comparable enhancement factors. However, from the viewpoint of stability against environments, Au is considered to be most preferable. Moreover, as shown in Fig. 9(b), the enhancement factor for Au for the z-polarized incident light had two peaks at around 430 and 520 nm. The enhancement factor at the wavelength of 430 nm was larger than that at the wavelength of 520 nm, but the absorption efficiency at the wavelength of 430 nm was also higher than that at the wavelength of 520 nm. Therefore, the wavelength of the incident light should be selected considering this trade-off relationship between the enhancement factor and the absorption efficiency.

5. Conclusions

The localized surface plasmons generated by the metal nano-dot in the novel device for the HAMR heat source were analyzed using a simple model in which a metal nano-hemisphere is formed on a GaAs substrate and the quasi-electrostatic approximation. The scattering and absorption efficiencies as well as the enhancement factor were investigated. As a result, their dependence on the wavelength and the polarization direction of the incident light was clarified. Future works include a more rigorous simulation instead of the quasi-electrostatic approximation as well as the consideration of the dependence of the dielectric constants on R. A simulation for a more complicated model that includes the recording medium in close proximity to the metal nano-dot needs to be conducted also as the next step. Moreover, the simulation can be extended to the case in which an incident light is focused on the metal nano-dot by expanding the incident light into plane waves with different polarization directions and adding the amplitudes of corresponding near-field lights.

References

1) M. H. Kryder, E. C. Gage, T. W. McDaniel, W. A. Challener, R. E. Rottmayer, G. Ju, Y.-T. Hsia, and M. F. Erden: Proc. IEEE **96** (2008) 1810.
2) W. A. Challener, C. Peng, A. V. Itagi, D. Karns, W. Peng, Y. Peng, X. Yang, X. Zhu, N. J. Gokemeijer, Y.-T. Hsia, G. Ju, R. E. Rottmayer, M. A. Seigler, and E. C. Gage: Nat. Photonics **3** (2009) 220.
3) B. C. Stipe, T. C. Strand, C. C. Poon, H. Balamane, T. D. Boone, J. A. Katine, J.-L. Li, V. Rawat, H. Nemoto, A. Hirotsune, O. Hellwig, R. Ruiz, E. Dobisz, D. S. Kercher, N. Robertson, T. R. Albrecht, and B. D. Terris: Nat. Photonics **4** (2010) 484.
4) K. Kuriyama, M. J. Chabalko, Y. Kong, Y. Lou, T. E. Schlesinger, and J. A. Bain: 12th Joint MMM-Intermag Conf., 2013, AB-01.
5) M. M. Wind, J. Vlieger, and D. Bedeaux: Physica A **141** (1987) 33.
6) *Handbook of Optical Constants of Solids*, ed. E. D. Palik (Academic Press, London, 1985) p. 275.